

Miniaturized short-wavelength infrared spectrometer for diffuse light applications

Tyler Westover^{Ⓧ, a, b, *} Zach Westhoff,^a Sharisse Poff,^c Nick Morrill,^b David Miller,^b Shih-Hua Wood Chiang^{Ⓧ, c}, Richard Vanfleet^{Ⓧ, a} and Robert Davis^a

^aBrigham Young University, Department of Physics and Astronomy, Provo, Utah, United States

^bTula Health Inc., Farmington, Utah, United States

^cBrigham Young University, Department of Electrical and Computer Engineering, Provo, Utah, United States

Abstract. A miniaturized short-wavelength infrared spectrometer for use with diffuse light was created by combining a thin form factor carbon nanotube composite collimator, a linear variable filter, and an InGaAs photodiode array. The resulting spectrometer measures 3 mm × 4 mm × 14 mm and shows a significant improvement in resolution over a spectrometer without the collimator when used with diffuse light. Its small size and high throughput make it ideal for applications such as wearable optical sensing, where light from highly scattering tissue is measured. Plethysmographic measurements on the wrist were demonstrated, showing rapid data collection with diffuse light.

Keywords: spectrometer; wearable optical sensing; short-wavelength infrared region.

Received Jun. 14, 2023; revised manuscript received Sep. 2, 2023; accepted for publication Sep. 28, 2023; published online Oct. 19, 2023.

© The Authors. Published by SPIE and CLP under a Creative Commons Attribution 4.0 International License. Distribution or reproduction of this work in whole or in part requires full attribution of the original publication, including its DOI.

[DOI: [10.1117/1.APN.2.6.066003](https://doi.org/10.1117/1.APN.2.6.066003)]

1 Introduction

Recent advancements in tissue measurements have enabled the widespread use of wearable health monitors. These monitors incorporate sensors to obtain and report a wearer's physiological data, with the goal of enabling more informed health decisions. More versatile miniature sensors can provide additional physiological information.^{1,2} One region of the optical spectrum with untapped potential for continuous measurement of physiological information is the short-wavelength infrared (SWIR),^{3,4} which typically incorporates 900 to 1700 nm light. In this region, there are key absorption peaks for biological molecules, such as glucose, urea, triacetin, and water.^{3,5,6} However, changes in these peaks cannot easily be isolated using traditional broad light-emitting diodes (LEDs) and a single photodiode, causing them to become confounding variables for one another. This presents the need for higher resolution data, a challenge that may be addressed by a miniaturized spectrometer.

Spectroscopy is an invaluable tool in better understanding materials and the chemical makeup of matter,⁷ including physiological concentrations of molecules. SWIR spectroscopy has

been applied to many fields, including tissue classification,⁸ food quality,⁹ soil testing,¹⁰ and recycling.¹¹ Recent research has been focused on both miniaturizing and reducing the cost of spectrometers to increase their availability and utility.^{12–16} Spectrometers use various methods to separate the light into composite wavelengths, including diffraction gratings,¹⁷ wedge filters,¹⁸ Fourier transform,¹⁹ metasurfaces,²⁰ and tunable filters.²¹ Each technique requires collimated light for optimal performance. Wedge filter-based spectrometers, which operate on the same principle as thin-film interference bandpass filters, have been studied as one route to spectrometer miniaturization.^{18,22–24} In a wedge filter, the interference layer thickness varies from one side to the other across the filter. This results in a passband center wavelength that varies with position. When the allowed wavelengths change linearly along the wedge, the filter is called a linear variable filter (LVF). When an LVF is combined with a linear photodiode array, each pixel in the array corresponds to specific wavelengths, resulting in a simple spectrometer.^{18,25}

LVF's resolution is highest when incoming light is collimated perpendicular to the surface of the filter. However, after passing through tissue, outgoing light is highly diffuse.³ This presents a challenge for LVF-based spectrometers, as the

*Address all correspondence to Tyler Westover, tyler.westover13@gmail.com

detected light is no longer perpendicular to the surface of the filter.²⁶ Other miniaturized spectrometer approaches also require collimation for high-resolution measurements. A collimator could be used to collimate the light prior to the spectrometer, but traditional lens- or aperture-based collimators require long optical path lengths, making them nonideal for miniaturized devices. One solution to this issue is to utilize parallel hole filters, a type of collimator that can be miniaturized. Parallel hole filters are densely packed arrays of high-aspect ratio tubes that geometrically limit light transmission to a small range of angles around normal incidence, i.e., off-axis light will pass through one end of the tube and be absorbed in the wall of the tube, but on-axis light will pass down the axis of the tube and exit the other side. With the aid of carbon nanotube templated micro-fabrication (CNT-M), we recently designed, fabricated, and tested a miniaturized collimator intended for spectrometer-based wearable optical monitoring.²⁷ CNT-M based collimators have a fairly simple fabrication process and naturally result in absorptive surfaces,²⁸ and they offer a significant reduction in size compared to traditional lens collimation, allowing miniaturization beyond what is currently on the market.

In this work, we present the design and characterization of a miniaturized SWIR spectrometer for diffuse light applications. Without the need of a grating or lenses, the spectrometer size was reduced to 3 mm × 4 mm × 14 mm. The spectrometer consists of a CNT-M collimator, an LVF, and a 128 pixel linear photodetector array (Fig. 1). The resulting resolution (full width half-maximum, FWHM) of 13 nm at 1300 nm, and the collimating characteristics are compared to that of an analytical optical model. The dark current noise was measured to be -28 dB. Additional calibrations, including dark current subtraction and bright-field correction, are discussed in the [Supplemental Material](#). In a

human subject experiment, the sensitivity of the miniaturized spectrometer was compared to that of a commercially available grating-based spectrometer (size, 88.9 mm × 63.5 mm × 31.9 mm) and found to have a throughput more than 100× higher. Using surface-mount LED illumination, the spectrometer was used to demonstrate the collection of high-quality plethysmographic signal from the radial artery of the wrist.

2 Materials and Methods

The carbon nanotube (CNT) collimator was manufactured using the CNT-M process, as described previously.^{27,29,30} Briefly, 70 nm of alumina was reactively sputter-coated onto silicon substrates. A CNT growth catalyst (4 nm of iron) was then deposited in a pattern onto the substrate using contact lithography, thermal iron evaporation, and liftoff. CNT forest growth with ethylene gas was performed on the catalyst-coated silicon substrates in a 2.54 mm tube furnace at 750°C. The growth time was 6 min to achieve the desired CNT growth height of 400 μm. Following growth, the CNT forest was infiltrated with carbon (10 min in ethylene at 900°C) to improve the strength of the CNT-M collimator. After growth and infiltration, the samples were exposed to an oxygen plasma for 10 min to remove excess carbon deposited on the substrate during infiltration and release the collimator from the substrate. CNT-M fabrication uses common semiconductor processing tools, and as such, would not be cost-prohibitive in relation to a more complicated part, such as the LVF or photodiode array.

The spectrometer was assembled using the CNT-M collimator, a LVF (Viavi Solutions), and a photodiode array (Hamamatsu G13913-128FB). All single spectrum data collection measurements from the Hamamatsu array were made using a development board and software provided by Hamamatsu.

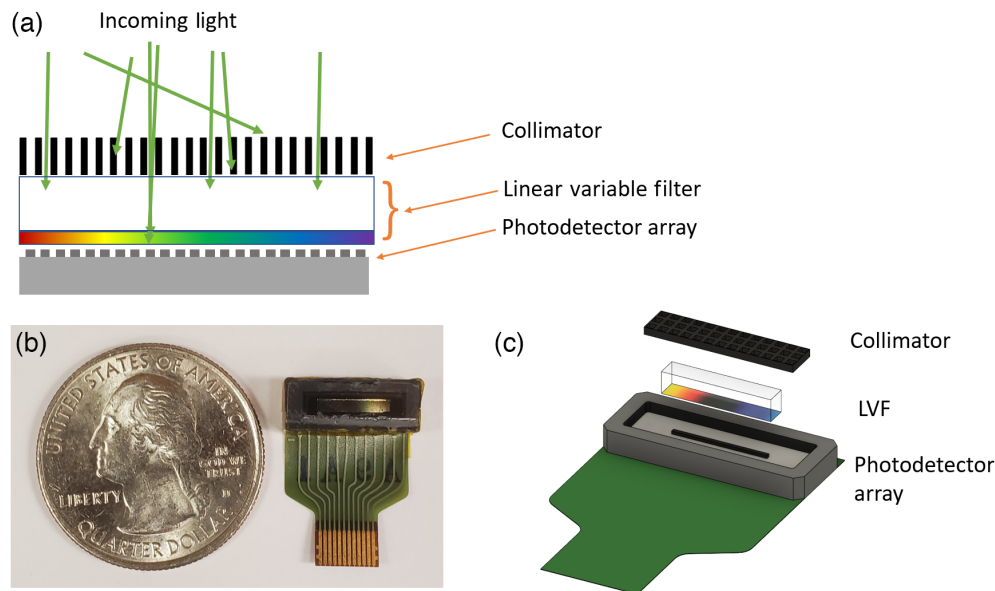


Fig. 1 Schematic view of the spectrometer assembly. (a) Monochromatic diffuse light enters spectrometer from the top. The light is collimated by the CNT collimator, separated by wavelength by the LVF and ultimately collected by the photodetector array. (b) Complete spectrometer compared in size to a quarter. A 3D printed holder contains the LVF and collimator and is sealed with a plastic window. The photodiode array is attached to a flexible substrate. Full spectrometer is compared to the size of a quarter. (c) CAD illustration of the collimator, LVF, and photodiode array. This exploded view shows the components without the 3D printed holder.

A 16-bit microcontroller-based (Teensy 3.5) data collection system was developed and used for longer runs and pulsatile data collection and was described previously.³¹ The collimator housings were designed using computer-aided design software (CAD) and 3D printed on the Formlabs Form 3 stereolithography printer using Formlabs standard black resin (Supplemental Material). To protect the collimator during spectrometer handling, a thin glass or plastic slide was cut and attached to the collimator housing using superglue. A CAD model of the assembly is shown in Fig. 1(c) (for illustration, the housing is not shown).

The spectrometer was constructed with dimensions of 3 mm × 4 mm × 14 mm and is shown in Fig. 1(b) alongside a U.S. quarter for scale. In this configuration, the spectrometer is connected to a flexible printed circuit board (PCB) for ease of testing, but it can also be directly mounted to a PCB. Figure 1(c)

shows a CAD model of an exploded view of the spectrometer, with the three main components arranged from top to bottom: the collimator, LVF, and photodiode array.

The resolution of the spectrometer was determined using the setup shown in Fig. 2(b). Monochromated light was provided by a tungsten filament light source and a monochromator (Spectral Products DK240), with a calculated spectral width of 2 nm based on the slit width used. Light exiting the monochromator was diffused using a diffusing mirror (Thorlabs DG10-1500) reflected onto a 100 deg engineered diffuser that was placed directly on the spectrometer [Fig. 2(b)]. Diffused light illuminated the full spectrometer, and the FWHM of the beam was measured. Resolution was measured every 100 nm starting at 1000 nm and ending at 1500 nm, both with and without the collimator, to determine its effect on spectral resolution and overall performance. The monochromatic light was dim and

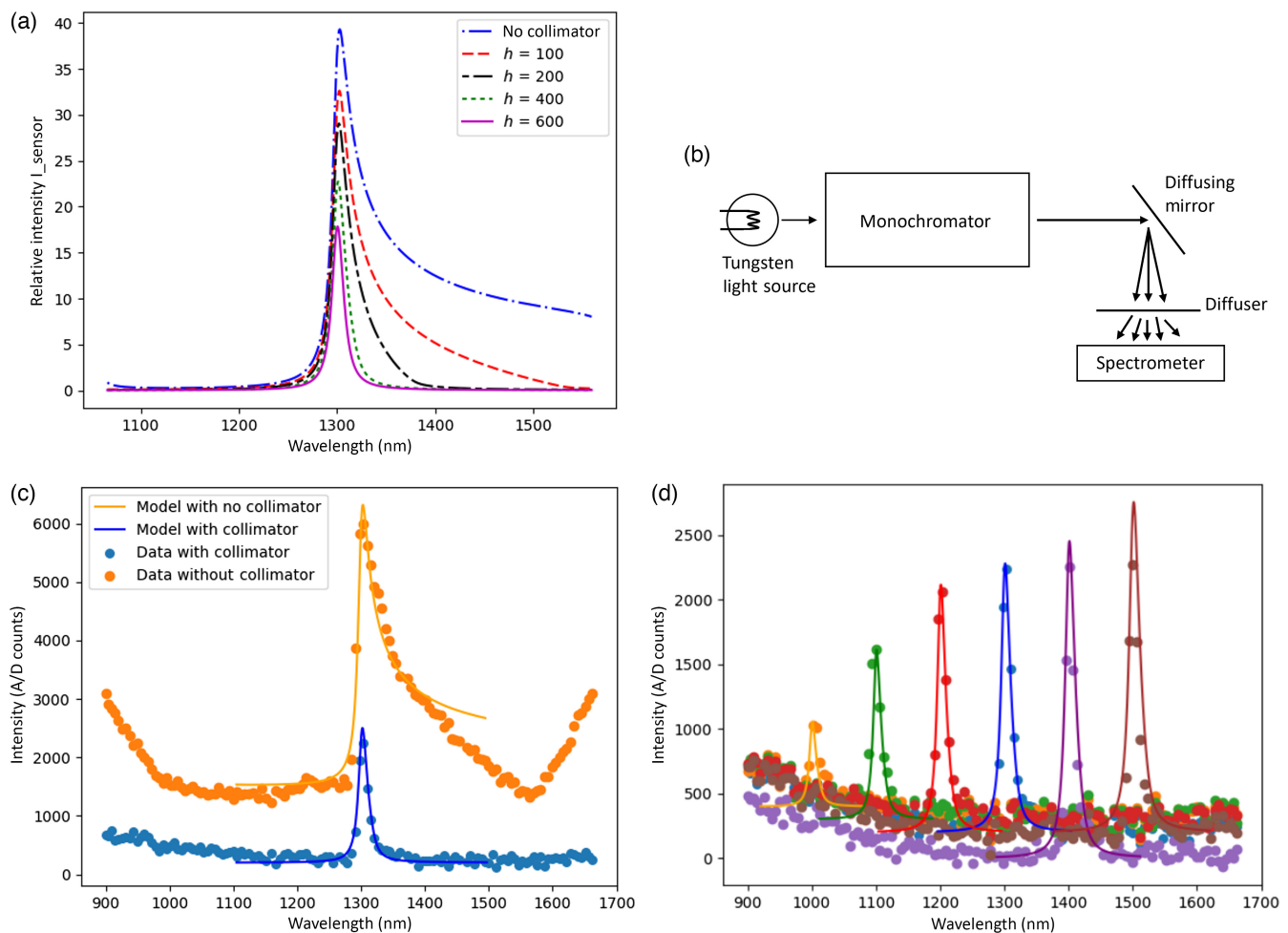


Fig. 2 Monochromated light exits the monochromator and is diffused first by a reflective diffuser and second, by an engineered diffuser that is immediately above the spectrometer. Data are collected with and without the collimator. (a) Modeled intensity distribution from the LVF-photodiode combination with 100 μm pore with 5 μm sidewalls and varying heights in μm . (b) Schematic of the experimental setup. (c) Spectrum of light taken by the spectrometer from monochromatic diffuse light with center wavelength at 1300 nm and an FWHM of 2 nm with a CNT-M collimator (orange dots) and without one (blue dots). The model in A is fit in amplitude and baseline which shows good agreement with the experimental results (solid line). (d) Diffuse light shone into the spectrometer at different wavelengths (dots), and the spectral response is plotted. At 1300 nm, the FWHM is about 13 nm, matching the expected resolution of the LVF (lines).

required an integration time of 0.5 s to get a clear signal. Dark current was collected by taking a spectrum when the illuminating light source was off and subtracted from each spectrum. Wavelength calibration was done by mapping photodetector pixels to monochromator center wavelength values, with linear interpolated values used for pixels between peaks.³²

To calibrate for the varied pixel-to-pixel responsivity, bright-field correction was performed by illuminating the spectrometer with a broad-spectrum tungsten halogen bulb. The collected spectrum was smoothed using a five-boxcar average. Each pixel from the smoothed spectrum was divided by the same pixel in the raw spectrum to get a gain correction ratio. This ratio was divided into future spectra as a bright-field correction. This process and the associated uncertainty are discussed further in the [Supplemental Material](#).

To characterize dark noise, dark current was measured in a temperature-controlled chamber for over 20 h. The charge from each pixel was converted to a voltage and all 128 pixels were recorded every 10 ms by the microcontroller. The 10 ms cycle time consisted of an 8.5 ms charge integration time and a 1.5 ms data readout time for the 128 pixels. The dark current noise was measured to be 6 A/D counts (−28 dB) and is plotted in the [Supplemental Material](#). The temperature dependence of the spectrometer dark current signal was measured by varying the chamber temperature in a controlled manner from 0°C to 40°C while collecting data with the nonilluminated spectrometer. This yielded a change of up to 1000 A/D counts, with the data shown and discussed further in the [Supplemental Material](#). The smoothing effect of bright-field and dark current corrections and their associated uncertainties on a spectrum is demonstrated and further discussed in the [Supplemental Material](#). Typical signals are tens of thousands of counts, so 1000 count dark levels are small but not ignorable. Data processing subtracts these dark levels. The spectrometer has been studied under a small range of normal operating conditions with no anomalous temperature effects. However, extreme temperature impacts the efficiency of the optical path or photodiode response have not been studied.

A human subject wrist-based test was performed to compare the throughput of the miniaturized spectrometer to that of a small commercially available grating-based SWIR spectrometer (Ocean Insight Flame NIR). The comparison measurement was a transmittance measurement on the wrist from a broadband tungsten source to the spectrometer. The tungsten source consisted of a 100-W tungsten bulb coupled to a 12 mm diameter, 0.9 m fiber-optic bundle. The fiber-optic bundles from the tungsten source and the Flame spectrometer were placed adjacent to each other on the skin of the wrist, approximately above the radial artery. A spectrum was collected using the Flame's automatic integration feature, which selected an integration time of 5500 ms. The Flame was then replaced by the miniaturized spectrometer at the same spacing and light intensity, and the experiment was repeated with an integration time of 30 ms, chosen to yield similar A/D counts across the spectrum.

Pulsatile measurements were performed using the miniaturized spectrometer coupled with LEDs (Marktech 1206 SMDs) in a single unit. Five LEDs were used with center wavelengths of 1050, 1300, 1550 nm, and two at 1650 nm. The LEDs were arranged linearly along the side of the spectrometer to locate them near the corresponding passband wavelength locations on the LVF, ~4 mm away from the edge

of the LVF. The spectrometer was placed on the wrist with the detector above the radial artery and the LEDs on the nearest tendon side of the artery. Once positioned over the artery, neither placement nor pressure was altered to optimize pulsatile amplitude. Data collection was performed using the microcontroller-based system using an integration time of 8.5 ms, with complete spectra collected every 10 ms for ~3 min. Human subject research in this study was done with approval from the institutional review board at Brigham Young University (IRB #F2020-268).

3 Theory

LVFs can be modeled as a series of Fabry–Pérot filters, which are thin-film interference filters used to isolate a narrow spectral band of light. The spectral passband is determined by the space between two thin-film mirrors, creating a cavity for resonant wavelengths to pass through. These filters are designed for collimated light to enter at near normal incidence. When diffuse light is used, the filter loses selectivity, allowing a much larger band of light through [Fig. 2(a)]. When incident light is off-normal, the path length of light is lengthened, allowing out-of-band wavelengths to pass. The CNT-M collimator limits higher angle incident light from passing to the LVF, thus retaining the wavelength selectivity of the LVF. Figure 2(a) shows the effect of a 100- μm wide collimator pore with varying heights (also see the [Supplemental Material](#)).

The model we use to calculate filter transmission combines three components: normal incidence transmission through a Fabry–Pérot cavity, the change in effective wavelength in the cavity due to angled incident light, and the limiting of angles by the collimator based on aspect ratio. Figure 2(a) shows the predictions of the model with no collimator and then with collimators of varying aspect ratios.

The Fabry–Pérot cavity model uses double reflectors separated by a gap with the assumption that the angle does not exceed the critical angle where light would be totally reflected. Transmission through a Fabry–Pérot filter at normal incidence is given in Eq. (1).³³ In our calculations, we use incident light that is unpolarized with a hard cut-off in angle at ± 50 deg,

$$T^{\text{tot}} = \frac{T^{\text{max}}}{1 + F \sin^2(\frac{\theta}{2})} \quad \theta = \frac{4\pi n_{\text{filter}} d}{\lambda_{\text{vac}}}, \quad (1)$$

where T^{Tot} is the total light transmitted through the filter, T^{max} is the max transmission possible by the filter (set to 50% based on minimum transmission given by manufacturer), F is the finesse coefficient calculated based on the specifications given of the filter (FWHM of about 1%), yielding a value of ~1000, n_{filter} is the index of refraction of the filter; it was assumed to be 1.33 as it was not provided by the manufacturer, d is the thickness of the cavity (distance between reflectors), and λ_{vac} is the wavelength of light incident on the filter in a vacuum. This equation assumes normal incidence transmission. The index of refraction and thickness of the cavity are a half-integer multiple of the expected pass-through wavelength ($n_{\text{filter}} d$ was set to the pass-through wavelength). In practice, LVFs include additional step filters to block wavelengths of nearby half-integer multiples of the pass-through wavelength. For simplicity, these multiples are ignored in this model, and

the wavelengths graphed in Fig. 2 are limited to our range of interest, which does not include these higher multiples.

With angled (off-normal) incident light, wavelengths longer than the normal incidence filter passband are transmitted. This out-of-band transmission degrades resolution, as seen in the no collimator and low-aspect-ratio collimator plots in Fig. 2(a). Angled light results in an “effective” cavity wavelength that is shorter than the actual light wavelength. Equation (2) maps the actual wavelength λ_{center} at incident angle θ_{in} to an effective pass-through wavelength λ_{eff} . λ_{eff} is used to replace $(n_{\text{filter}} d)$ in Eq. (1) to calculate angled light transmission,

$$\lambda_{\text{eff}} = \lambda_{\text{center}} \left(1 - \frac{1}{n_{\text{filter}}} \sin^2 \theta_{\text{in}} \right)^{1/2}. \quad (2)$$

The collimator impacts transmission in two ways. First, it causes shadowing loss due to decrease in open area, i.e., the collimator walls block a fraction of the light from passing, even at normal incidence. Second, it reduces the allowed angles that can pass through the collimator. This is determined by geometric optics and the aspect ratio (ratio of height to pore width), as shown in Eq. (3). The higher the aspect ratio, the more limited the allowed angles that can enter the LVF,

$$\Theta = \text{ArcTan} \left[\frac{\text{porewidth}}{\text{height}} \right]. \quad (3)$$

4 Results

The spectral resolution of the spectrometer was characterized with diffuse light to simulate the high level of scattering that occurs when measuring body tissue. Tests were performed with and without collimation to show the collimator’s effect on the spectral resolution. The collected spectrum shown in Fig. 2(c) is from illumination by a narrow-wavelength band light source centered at 1300 nm and diffused prior to detection by the spectrometer. The transmission is shown without a collimator (plotted in orange dots) and with a collimator (plotted in blue dots), with model predictions added for comparison. The amplitude and baseline offset for the model were fit to the measured data using a fitting method of determining the scalar for the amplitude that minimizes the distance between the data points and the model (lines). The no-collimator and with-collimator data sets match the model at the center wavelength with a sharp transmission peak. The no-collimator measured data set exhibits the same features as the model with the sharp peak at the center wavelength and an additional right-sided tail. The baseline of the result without a collimator is much higher than that of the collimator measurements and the theoretical model. The measured no-collimator results also have peaks at the edges of the spectrum not shown in the model. With the collimator in place, the peak decreases rapidly and no other features are detected; the resolution of the spectrometer matches that specified by the LVF manufacturer 1% of the pass-through wavelength, or 13 at 1300 nm.

To test resolution at multiple wavelengths, the center wavelength was varied in 100 nm steps from 1000 to 1500 nm; the resulting collimated spectra are shown as dots in Fig. 2(d). Model predictions are plotted in solid lines and the amplitude and baseline offset of the model were fit to the data. The resolution of the spectrometer was measured by determining the

FWHM when the collimator was in place [Fig. 2(d)]. The data for the longer wavelengths (1200 to 1500 nm) have similar intensities and a resolution of about 1% of the center wavelength. The measured intensities of the 1000 and 1100 nm peaks are lower than those of the longer wavelengths. The baseline signals of the measurements all seem to increase near the 900 nm side of the spectrometer, which may be due to a small light leak on that side of the LVF.

A tissue transfectance measurement was performed using the miniaturized spectrometer in comparison to a commercially available grating-based SWIR spectrometer. The spectra from two spectrometers, when illuminated on the wrist, were collected at different integration time to show the differences in throughput in a wearable application. The resulting data are shown in Fig. 3. To obtain similar A/D counts as measured on both spectrometers, the grating-based spectrometer had an integration time of 5500 ms, while the miniaturized spectrometer had an integration time of 30 ms. The grating-based spectrometer’s spectrum is significantly noisier, likely due to the long integration time. No bright- or dark-field corrections are applied to the miniaturized spectrometer for this comparison. Although illuminated with a broad light source, both spectra have a large peak at about 1050 nm and a second small peak at about 1300 nm. In the miniaturized spectrometer, there appears to be a peak start at 1650 nm.

Plethysmographic spectra were taken on the wrist with the spectrometer placed over the radial artery and the LEDs on the tendon side on the wrist (Fig. 4). An LED board was glued to the 3D printed housing of the spectrometer. A wrist strap, as shown in Fig. 4, was used to hold the spectrometer in place. Cables for the spectrometer and LEDs came out the side of the spectrometer module. Data were collected using the microcontroller for several minutes. A 7.5 s segment of those data for the 1050 nm pixel is shown in Fig. 4. The pulsatile variation in the data shown sits on the 51,000-count background shown in the vertical scale.

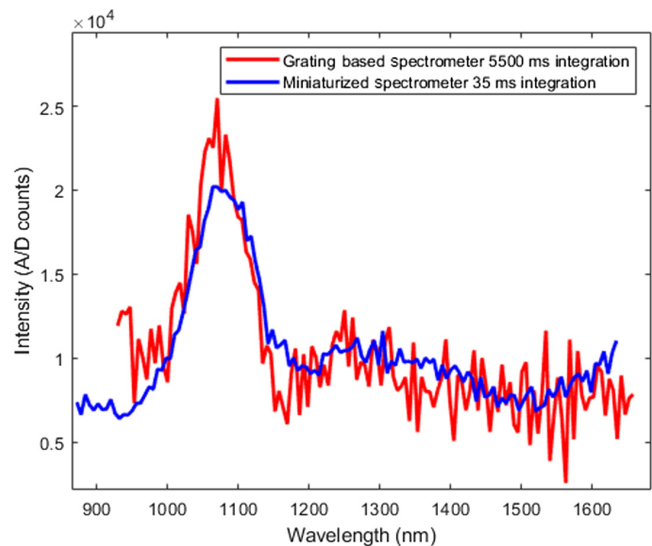


Fig. 3 Spectrum measured on the wrist with both a grating-based SWIR spectrometer and our miniaturized spectrometer. The integration time was varied to get the same A/D counts on both devices. The grating-based spectrometer integrated from 5500 ms while the miniaturized spectrometer integrated from 30 ms.

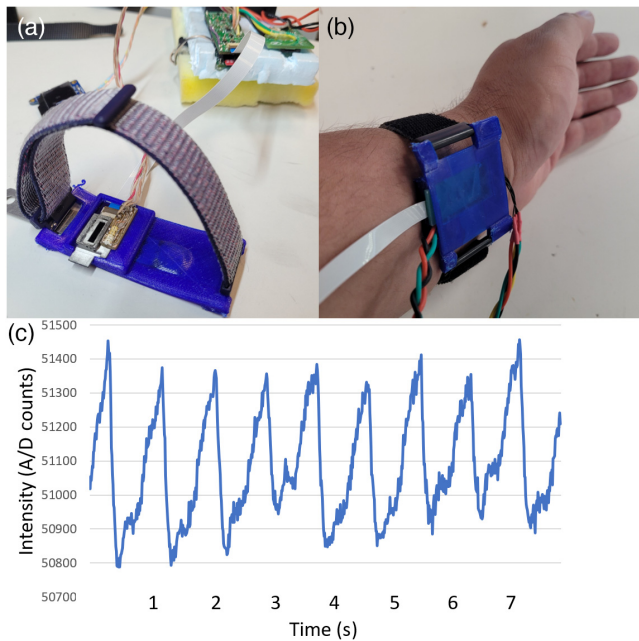


Fig. 4 A pulse measured on the wrist. (a) Photo of the spectrometer used on the wrist. (b) The spectrometer was placed directly over the artery with the LEDs placed on the tendon side of the arm. (c) A series of spectra are collected at 10 ms intervals, and the pixel corresponding to 1050 nm is plotted in time, yielding a pulsatile waveform. The 1050 nm peak is chosen to illustrate the pulse due to its large pulsatile amplitude.

5 Discussion

The advantage of a CNT-M collimator in a compact spectrometer has been demonstrated both theoretically and experimentally with diffuse light. The chief advantage of the collimator for an LVF-based spectrometer is its small size, while significantly improving diffuse light resolution. For the spectrometer data shown in Fig. 2(c), the resolution (the FWHM) improves from ~ 60 nm without a collimator to ~ 13 nm with a collimator. This improvement is achieved by allowing a narrower range of angles into the LVF, as the width of the LVF passband is smallest for near-normal incident light. The collimator limits off-normal incident light by blocking the transmission beyond the collimator cut-off angle, which is determined by the pore size and height of the collimator.

Increasing the aspect ratio of the collimator pores can improve resolution up to a certain point but reduces light throughput. The Fabry-Pérot filter model can help choose the desired trade-off between throughput and resolution. As shown in Fig. 2(a), peak intensity decreases with collimator height, while resolution increases. The model calculates passband width from two factors: 1) the normal incidence resolution inherent to the Fabry-Pérot cavity and 2) the angular broadening due to non-normal incident light. For narrower cut-off angles, angular broadening has less impact on resolution. However, below a certain cut-off angle, γ further reduction does not improve resolution. This occurs when the resolution is limited by the inherent normal incidence resolution of the LVF. As shown in Fig. 2(a), going from 400 to 600 μm (with a pore size of 100 μm) results in a minimal gain in resolution but significant reduction in light throughput. A collimator with a height of 400 μm and pore size of 100 μm , resulting in a cut-off angle of 14.3 deg, gave the

largest throughput without compromising resolution. We called this the optimized collimator.

The resolution of the miniaturized spectrometer with the optimized collimator compared well against the inherent normal incidence resolution of the LVF across its spectral range. The LVF specifications give a normal incidence FWHM resolution of $<1\%$ of the pass-through center wavelength; we will call this the “LVF limited resolution.” The spectrometer’s resolution at near-normal incidence was measured with non-diffuse light using a krypton calibration source (details in the [Supplemental Material](#)), resulting in a 13 nm FWHM, matching the LVF specification (e.g., 1% gives 13 nm FWHM at 1300 nm). With diffuse light and the optimized collimator, we showed a resolution essentially matching the “LVF limited resolution” across the spectrometer’s spectral range [Fig. 2(d)].

There was found to be good agreement between the collimation theoretical models and experimental results. Two main artifacts were identified in the transmission data collected without a collimator: a significant baseline signal across the entirety of the spectrum and a sharp rise in signal at the ends of the spectrum, one near 900 and the other near 1650 nm [see Fig. 2(c)]. Although these artifacts were significantly reduced with the collimator, we will discuss their possible origin. The baseline signal may be due to off-normal incidence light bypassing the LVF (leaking around the sides of it) and illuminating the photodiode array without passing through the filter. The rise in signal seen at the edges of the spectrum may likewise be due to non-normal light leakage around the physical edges of the LVF. The collimator cuts off most off-normal incident light, minimizing these light-leakage-based artifacts.

Outside the peak in each spectrum of Fig. 2(d), the A/D counts exhibit a fairly constant baseline across each spectrum (except for wavelengths shorter than 1150 nm). However, there is a drift in this baseline as subsequent spectra are taken. The total drift was about 500 counts from the first to the last. The order of spectra taken was 1400, 1500, 1300, 1200, 1100, and 1000 nm. We attribute the baseline drift to an increase in dark current with temperature as the InGaAs sensor warms up, consistent with the measured temperature dependence of the dark ([Supplemental Material](#)). All spectra show elevated current at wavelengths shorter than 1150 nm, which increases as we approach the short-wavelength edge of the spectrometer. We attribute this elevated current to light leakage around the short-wavelength edge of the spectrometer constructed to obtain the comparison data shown in Fig. 2. This particular spectrometer was designed with a removable collimator, making it more difficult to control light leakage, but not compromising the comparison.

In human subject testing (Fig. 3), our miniaturized spectrometer demonstrated a 100-fold increase in throughput compared to the commercial grating-based IR spectrometer. Grating-based spectrometers have built-in collimation to allow for use in diffuse light measurements, but result in larger size. We attribute this improvement to the differences in optical components between the two technologies. We do not know the specific inner workings of the commercial grating-based spectrometer, and the losses could be due to the various optical components, including the grating,¹⁷ resulting in long integration time (5500 ms) for this diffuse light application. In contrast, our miniaturized spectrometer has fewer optical components and only experiences losses due to the LVF and collimator, allowing for significantly reduced integration time (30 ms). This is particularly important

for plethysmographic measurements, where multiple spectra must be collected within a single cardiac cycle.

Our miniaturized spectrometer has demonstrated the ability to collect plethysmographic data by measuring pulsatile waveforms. Despite the relatively small amplitude of the measured pulse compared to the non-pulsatile portion of the signal (600 A/D counts peak-to-peak pulsatile versus ~51,000 A/D counts of the non-pulsatile offset), we did not alter placement or pressure to optimize pulsatile amplitude once the spectrometer was placed generally over the artery. The 1050 nm peak was chosen to illustrate the pulse due to its high signal and large pulse, serving as a reference for finding the pulse at other wavelengths with lower signals.

We demonstrated the ability to measure plethysmographic data by collecting pulsatile waveforms with the miniaturized spectrometer. The pulsatile amplitude was relatively small compared to the non-pulsatile portion of the signal (600 A/D counts peak-to-peak pulsatile versus ~51,000 A/D counts of the non-pulsatile offset).

6 Conclusions

We have designed and characterized a miniaturized SWIR (900 to 1650 nm) spectrometer for diffuse light applications. This SWIR spectrometer measured 3 mm × 4 mm × 14 mm. This device is the smallest diffuse light SWIR spectrometer currently available. This small size could allow for more consumer-level applications in measuring food quality and soil analysis. Using a CNT-M collimator, the spectrometer can filter out diffuse light and achieve a spectroscopic resolution of 13 nm FWHM at 1300 nm, matching the LVF manufacturer specifications. Human subject measurements were performed under IRB protocols and showed that the miniaturized spectrometer had a throughput over 100 times higher than a grating-based spectrometer in wrist-based measurements. Using LEDs, we collected a pulse on an individual. Further customization of individual components, such as using thinner glass on the LVF, could reduce its size even more. The quality of physiological measurements made by the miniaturized spectrometer demonstrates its potential for use in wearable configurations to collect biometric data.

Data Availability

Data used to generate information in this paper can be found at <https://github.com/twestover13/Miniaturized-Spectrometer-for-diffuse-light>.

Acknowledgments

This research was partially supported and funded through Tula Health Inc. and Brigham Young University (BYU). We would like to thank the BYU microscopy and cleanroom facilities for their support and help. We would also like to thank Bryce Lunceford with help fitting the model to the data for Figs. 2(c) and 2(d).

References

- D. Lupton, "The digitally engaged patient: self-monitoring and self-care in the digital health era," *Social Theory Health* **11**(3), 256–270 (2013).
- A. Pantelopoulou and N. G. Bourbakis, "A survey on wearable sensor-based systems for health monitoring and prognosis," *IEEE Trans. Syst., Man, Cybern., Part C (Appl. Rev.)* **40**(1), 1–12 (2009).
- A. K. Amerov et al., "Scattering and absorption effects in the determination of glucose in whole blood by near-infrared spectroscopy," *Anal. Chem.* **77**(14), 4587–4594 (2005).
- I. Yusoff et al., "Non invasive cholesterol meter using near infrared sensor," in *Innov. & Commercialization of Med. Electron. Technol. Conf. (ICMET)*, IEEE, pp. 100–104 (2015).
- D. D. Cunningham and J. A. Stenken, *In Vivo Glucose Sensing*, John Wiley & Sons (2009).
- A. K. Amerov et al., "The influence of glucose upon the transport of light through the whole blood," *Proc. SPIE* **5330**, 101–111 (2004).
- J. M. Hollas, *Modern Spectroscopy*, John Wiley & Sons (2004).
- U. Dahlstrand et al., "Extended-wavelength diffuse reflectance spectroscopy with a machine-learning method for *in vivo* tissue classification," *PLoS One* **14**(10), e0223682 (2019).
- K. B. Beć, J. Grabska, and C. W. Huck, "Miniaturized NIR spectroscopy in food analysis and quality control: promises, challenges, and perspectives," *Foods* **11**(10), 1465 (2022).
- B. G. Barthès et al., "Performance comparison between a miniaturized and a conventional near infrared reflectance (NIR) spectrometer for characterizing soil carbon and nitrogen," *Geoderma* **338**, 422–429 (2019).
- M. Rani et al., "Miniaturized near-infrared (MicroNIR) spectrometer in plastic waste sorting," *Materials* **12**(17), 2740 (2019).
- T. S. Yeh and S. S. Tseng, "A low cost LED based spectrometer," *J. Chin. Chem. Soc.* **53**(5), 1067–1072 (2006).
- Z. Yang et al., "Miniaturization of optical spectrometers," *Science* **371**(6528), eabe0722 (2021).
- K. B. Beć et al., "Handheld near-infrared spectrometers: where are we heading?" *NIR News* **31**(3–4), 28–35 (2020).
- J. Zhang et al., "Cascaded nanobeam spectrometer with high resolution and scalability," *Optica* **9**(5), 517–521 (2022).
- G. Y. Belay et al., "Miniaturized broadband spectrometer based on a three-segment diffraction grating for spectral tissue sensing," *Opt. Lasers Eng.* **134**, 106157 (2020).
- F. Kneubühl, "Diffraction grating spectroscopy," *Appl. Opt.* **8**(3), 505–519 (1969).
- M. Dami et al., "Ultra compact spectrometer using linear variable filters," *Proc. SPIE* **10565**, 1056559 (2018).
- J. Ekkers and W. Flygare, "Pulsed microwave Fourier transform spectrometer," *Rev. Sci. Instrum.* **47**(4), 448–454 (1976).
- J. Xiong et al., "Dynamic brain spectrum acquired by a real-time ultraspectral imaging chip with reconfigurable metasurfaces," *Optica* **9**(5), 461–468 (2022).
- V. Saptari and K. Youcef-Toumi, "Design of a mechanical-tunable filter spectrometer for noninvasive glucose measurement," *Appl. Opt.* **43**(13), 2680–2688 (2004).
- N. A. O'Brien et al., "Miniature near-infrared (NIR) spectrometer engine for handheld applications," *Proc. SPIE* **8374**, 837404 (2012).
- B. Wiesent, D. Dorigo, and A. Koch, "3.3-A miniaturized MID-IR-spectrometer based on a linear variable filter and pyroelectric line array—monitoring oil condition," in *Proc. IRS² 2013*, pp. 59–64 (2013).
- A. Emadi et al., "Design and implementation of a sub-nm resolution microspectrometer based on a linear-variable optical filter," *Opt. Express* **20**(1), 489–507 (2012).
- B. R. Wiesent, D. G. Dorigo, and A. W. Koch, "Limits of IR-spectrometers based on linear variable filters and detector arrays," *Proc. SPIE* **7767**, 77670L (2010).
- L. Zhang et al., "Miniature spectrometer based on linear variable interference filters," *Proc. SPIE* **3855**, 42–50 (1999).
- T. Westover et al., "Visible and short-wavelength infrared light collimation through carbon nanotube, parallel-hole collimators," *Opt. Express* **30**(13), 22679–22686 (2022).

28. K. Laughlin, R. R. Vanfleet, and R. C. Davis, "Mechanically robust vertically aligned carbon nanotube composites for applications in ultralow reflectance optical elements," *ACS Appl. Nano Mater.* **5**, 6989–6994 (2022).
29. G. Chen et al., "Fabrication of high aspect ratio millimeter-tall free-standing carbon nanotube-based microelectrode arrays," *ACS Biomater. Sci. Eng.* **4**(5), 1900–1907 (2018).
30. W. C. Fazio et al., "Material properties of carbon-infiltrated carbon nanotube-templated structures for microfabrication of compliant mechanisms," in *ASMEDC* (2011).
31. Z. A. Westhoff, *Microcontroller-Integrated Miniature Infrared Spectrometer for Noninvasive Sensing of Physiological Signals*, Brigham Young University (2021).
32. A. Kenda et al., "Development, characterization and application of compact spectrometers based on MEMS with in-plane capacitive drives," *Proc. SPIE* **9101**, 910102 (2014).
33. M. Ware and J. Peatross, *Physics of Light and Optics* (2015).

Biographies of the authors are not available.